ACCSCIENCE PUBLISHING

International Journal of Bioprinting

RESEARCH ARTICLE

3D-printed PETG/BC scaffolds for bone tissue repair

Evangelos Daskalakis[1,2†*], Mohamed H. Hassan[2†*], Abdalla M. Omar[2†], Maria Kapousidou[3], Dino Freitas[1], Mehmet Cagirici[1], Cian Vyas[1], Hussein Mishbak[4], Alexandra Lanot[5], Niel C. Bruce[5], Prasad Potluri[3,6], Wajira Mirihanage[3], and Paulo J.D.S. Bartolo[1*]

[1]Singapore Centre for 3D Printing, School of Mechanical and Aerospace Engineering, Nanyang Technological University, Singapore, Singapore

[2]Department of Mechanical, Aerospace, and Civil Engineering, University of Manchester, Manchester, United Kingdom

[3]Department of Materials, The University of Manchester, Manchester, United Kingdom

[4]Department of Biomedical Engineering, School of Engineering, University of Thi Qar, Nasiriyah, Iraq

[5]Centre for Novel Agricultural Products, Department of Biology, University of York, York, United Kingdom

[6]Northwest Composites Centre and Aerospace Research Institute, Department of Materials, Faculty of Science and Engineering, The University of Manchester, Manchester, United Kingdom

[†]These authors contributed equally to this work.

***Corresponding authors:**
Evangelos Daskalakis (daskalakis.evangelos@ntu.edu.sg)

Mohamed H. Hassan (Mohamed.hassan@manchester.ac.uk)

Paulo J.D.S. Barrtolo (pbartolo@ntu.edu.sg)

Citation: Daskalakis E, Hassan MH, Omar AM, *et al.* 3D-printed PETG/BC scaffolds for bone tissue repair. *Int J Bioprint*. 2026;12(1):413-431. doi: 10.36922/IJB025210212

Received: May 21, 2025
Revised: July 10, 2025
Accepted: July 15, 2025
Published online: July 16, 2025

Abstract

Bone tissue supports the body, enables movement, protects organs, produces blood cells, and stores minerals. In regenerative medicine, bone's natural healing ability drives the need for engineered solutions to treat fractures, defects, and support implants. This study explores the development of polyethylene terephthalate glycol (PETG) and PETG/bacterial cellulose (BC) composite scaffolds with varying BC contents (10, 15, and 20 wt%) for bone tissue engineering (TE). Scanning electron microscopy and atomic force microscopy revealed porous structures with increasing surface roughness as BC content increased. Water contact angle analysis revealed enhanced hydrophilicity in PETG/BC composites, particularly at higher BC levels. Fourier transform infrared spectroscopy, X-ray diffraction, and differential scanning calorimetry confirmed successful BC integration and interactions with PETG, along with increased crystallinity. Mechanical testing indicated that compressive strength improved with higher BC content, with 20 wt% BC achieving optimal performance. Biological tests using human adipose-derived stem cells displayed enhanced proliferation, differentiation, and mineralization on PETG/BC scaffolds. Among the tested BC scaffolds, the 20 wt% BC scaffold demonstrated the most favorable physical, mechanical, and biological properties. Overall, PETG/BC scaffolds, especially those with 20 wt% BC, display strong potential for future bone TE applications.

Keywords: Additive manufacturing; Bacterial cellulose; Biomaterial; Polyethylene terephthalate glycol; Stem cells; Tissue engineering

1. Introduction

Tissue engineering (TE) integrates biological sciences with engineering strategies to create solutions that restore, support, or enhance tissue or organ function. It involves two principal strategies: the scaffold-based method and the cell-laden approach.[1,2] The scaffold-based approach, commonly applied in bone TE, utilizes 3D, biodegradable, and biocompatible porous structures that support cell adhesion, differentiation, and proliferation within a suitable biomechanical environment.[3,4] For successful applications, the scaffold degradation rate must match the tissue regeneration rate, and the scaffolds should exhibit high porosity and pore interconnectivity. These scaffolds should promote cellular function while ensuring adequate mechanical strength and rigidity to endure the stresses present in the host tissue environment. Moreover, they must exhibit appropriate surface properties (*e.g.*, chemistry, hardness, roughness, stiffness) to promote cell adhesion and adequate biomechanical coupling between the scaffolds and host tissue.[5,6]

Various biodegradable materials have been utilized for scaffold fabrication, including inorganic, organic, and composite materials.[7] A commonly used material in TE is polycaprolactone (PCL), which is an aliphatic polyester and has demonstrated promising results in bone applications. Scaffolds made from PCL with different porosities have been reported to support osteoblast and mesenchymal stem cell adhesion, contributing to osteogenesis and bone development.[8,9] Additionally, several studies demonstrated the effective application of PCL scaffolds in repairing critical-sized calvaria defects in rats, facilitating new tissue formation.[10] Despite its advantages, PCL presents weak bioactivity, low strength, and slow degradation, limiting its use in load-bearing bone repair.[2] To address these challenges, our group explored polyethylene terephthalate glycol (PETG), an aliphatic polyester, and demonstrated its effectiveness in bone applications.[11] PETG is a glycol-modified derivative of polyethylene terephthalate (PET), engineered to reduce the melting temperature and enhance printability. In comparison to PCL, PETG has higher mechanical properties and bioactivity.[11] However, the mechanical properties of PETG are still lower than those of cortical bone ; as a consequence, PETG scaffolds may not provide the necessary structural integrity for load-bearing applications, such as cortical bone regeneration.[12] Additionally, PETG lacks controlled degradation, which can hinder the natural healing process and integration of the scaffold.[13]

Bacterial cellulose (BC), produced by specific bacteria such as *Acetobacter xylinum*, is among the most abundant and renewable natural polymers found on the planet, with an estimated 100 –150 billion tons of cellulose produced globally each year.[14,15] BC has been widely used in various applications, including structural reinforcement, paper making, textiles, and biomedicine, owing to its fibrous morphology, low production costs, abundance, and biocompatibility.[16,17] These characteristics make BC a potential ideal reinforcement material for PETG scaffolds, overcoming the limitations previously mentioned.[18] Moreover, the natural hydrophilicity of BC could have a potential positive impact on cell attachment.[19] Additionally, the faster degradation of BC can compensate for the slow degradation rate of PETG, allowing the design of scaffolds with tunable degradation profiles.[20] Although no direct studies on BC/PETG composites are currently available, related work has demonstrated that incorporating BC into polylactic acid (PLA) matrices results in significantly enhanced degradation behavior. For example, PLA/BC scaffolds displayed approximately 18.75% mass loss in simulated body fluid over 6 weeks, compared to 14.38% for pure BC, while maintaining suitable mechanical stability for TE applications.[21,22] Similarly, BC has been used in composites with hydroxyapatite, chitosan, and polyvinyl alcohol, demonstrating improved biodegradability and mechanical performance tailored to bone tissue regeneration.[23,24] BC has also been reported to enhance osteoblast adhesion and proliferation, particularly when used in composites with bioceramics like hydroxyapatite, promoting osteoinduction and bone regeneration.[25] Furthermore, modification techniques, such as nanoparticle incorporation or surface patterning, have been successfully used to improve BC's mechanical and bio-functional properties for bone tissue applications.[26] The combination of PETG and BC can potentially produce scaffolds with better mechanical properties, degradation profiles, and biocompatibility.

This work investigates the use of BC as a potential reinforcement for PETG scaffolds. Various percentages of BC were mixed with PETG and analyzed using different techniques to assess the impact of BC on the physicochemical and biological properties of PETG scaffolds.

2. Materials and methods

2.1. Materials

PETG filament, with a diameter of 1.75 mm, was purchased from RS Components Ltd. (UK). *Gluconacetobacter xylinus* bacterial strain American Type Culture Collection (ATCC) 53524 was purchased from the bioresource center of the ATCC (USA). MesenPRO RSTM basal medium, growth supplement, glutamine, penicillin, the STEMPRO osteogenesis differentiation kit, bicinchoninic acid (BCA) Protein Assay Kit (Micro BCA), Alexa Fluor 594-conjugated phalloidin, 4′,6-diamidino-2-phenylindole

(DAPI), and Dulbecco's phosphate-buffered saline (PBS) were sourced from Thermo Fisher Scientific (UK). Bacterial peptone, yeast extract, disodium phosphate, citric acid monohydrate (with 2% glucose), Triton X-100, hexamethyldisilane (HMDS), and formaldehyde were purchased from Sigma-Aldrich (UK). The MTT Cell Proliferation Assay Kit was provided by Abcam (UK), and the SensoLyte® NPP Alkaline Phosphatase (ALP) Assay Kit was supplied by AnaSpec (Eurogentec, Belgium).

2.2. Bacterial cellulose production

BC was produced using *Komagataeibacter xylinus* ATCC 53524 (ATCC, USA). The strain was cultured in Hestrin–Schramm medium that contains 50 g/L bacterial peptone, 50 g/L yeast extract, 27 g/L disodium phosphate, and 15 g/L citric acid monohydrate in the presence of 2% glucose.[27] The bacteria were cultured at 30 °C under static conditions. After 6 days, the cellulose pellicles were harvested, incubated at 80 °C for 4 h in 0.1 M sodium hydroxide, and then air-dried after extensive washing with deionized water. Finally, dried cellulose pellicles were milled using a ball mill at a frequency of 30 s^{-1} for 1 min (TissueLyserII, Qiagen, Germany).

2.3. Filament production

The PETG filaments were pelletized (4 mm) using the Process 16 Pelletizer (Thermo Fisher Scientific, UK). Simultaneously, BC powder and PETG pellets were fed, in a controlled manner, into two different Twin Screw Brabender feeders (Kubota Brabender Technologie GmbH, Germany), and then passed through the Haake Polylab Rheomex Twin Screw Extruder (Thermo Fisher Scientific, UK), heated at 190 °C, to melt the polymers and extrude them into a strand. The mixed PETG/BC strand was pulled through a water bath to reduce the temperature of the material. The cooled strand was then fed into the pelletizer, producing 4 × 1.75 mm (length × diameter) pellets. The procedure was repeated for the production of three different concentrations of PETG/BC (90/10, 85/15, and 80/20 wt%). In order to achieve an accurate mixing between BC and PETG, it was important to determine the volumetric flow rate (**Equation I**) and gravimetric flow rate (**Equation II**):

$$VF = \frac{Q}{\rho} \quad \text{(I)}$$

$$GF = \frac{m}{t} \quad \text{(II)}$$

where VF is the volumetric flow rate, Q is the feed rate, ρ is the density of the polymer, GF is the gravimetric flow rate, m is the mass of the polymer, and t is the duration of the flow. Table S1 presents the VF and GF results for the different material concentrations. After the mixing process, the pellets were left to dry inside an oven at 50 °C for 48 h. The dried pellets were extruded using the 3Devo filament maker (3Devo, Netherlands) at 190 °C, producing 1.75 mm filaments.

2.4. Fabrication process

Scaffolds were fabricated using Prusa i3 MK3S (Prusa Research, Czech Republic) at 210 °C. Scaffolds of different material concentrations were fabricated with dimensions of 30 × 30 × 5 mm (length × width × height) and subsequently cut into smaller pieces for compression tests, according to the ASTM D695-15 standard.

2.5. Morphological characterization

The morphology of the 3D-printed scaffolds was examined using scanning electron microscopy (SEM) (FEI Quanta 650, FEI Company, USA). Prior to imaging, a 10-nm layer of platinum/palladium (80:20) was applied using an EMITECH K550X sputter coater (Quorum Technologies, UK). ImageJ was used for the analysis of top and cross-sectional images of the 3D-printed scaffolds. The gravimetric method was used to calculate scaffold porosity ($n = 4$) as follows:

$$Porosity\,(\%) = \left(1 - \frac{\rho_s}{\rho_m}\right) \times 100 \quad \text{(III)}$$

with

$$\rho_s = \frac{m_s}{v_s} \quad \text{(IV)}$$

where ρ_s is the apparent density of the scaffold, ρ_m is the density of the PETG/BC scaffold, m_s is the measured mass of the scaffold, and v_s is the volume of the scaffold. The theoretical densities of PETG and BC are 1.27 and 1.6 g/cm^3, respectively.[28,29]

2.6. Surface morphology

Atomic force microscopy (AFM) characterization was performed using the ScanAsyst mode (Bruker Optik GmbH, UK), with ScanAsyst Air silicon nitride probes, 70 KHz nominal frequency, 0.4 N/m spring constant, and 2 nm nominal tip radius. Using Bruker data analysis software (Bruker Optik GmbH, UK), all images were flattened, and the background was subtracted.

2.7. Wettability

Water contact angle (WCA) measurements were carried out using a CAM 200 Optical Contact Angle Meter with an integrated goniometer (KSV CAM 200, Leuven,

Finland). Deionized water droplets were dispensed onto the scaffold surface, and contact angle images were recorded immediately (0 s) and after 1 min to assess temporal changes.

2.8. Rheology

Rotational and oscillation tests were conducted using the Discovery HR-3 Rheometer (TA Instruments, USA). A steel parallel plate (diameter = 20 mm) with a gap of 450 μm was used for testing the different material blends (n = 3). The printing temperature of pure PETG filaments is typically between 190 and 210 °C; therefore, three temperatures were selected for rheological evaluation (190, 200, and 210 °C). A constant strain of 1% and a frequency of 10 –0.01 Hz were used for the logarithmic sweep in the oscillation test, while a shear rate of 0.01– 100 s^{-1} was applied for the logarithmic sweep in the rotational test. The viscoelastic properties of the blends were evaluated by measuring the storage modulus (G′) and loss modulus (G″), representing the elastic and viscous responses, respectively. Storage and loss moduli were calculated using the following equations:

$$G' = \left(\frac{\sigma_o}{\gamma_o}\right) \times cos\delta \quad \text{(V)}$$

$$G'' = \left(\frac{\sigma_o}{\gamma_o}\right) \times sin\delta \quad \text{(VI)}$$

where σ_o is stress amplitude, γ_o is strain amplitude, and δ is the phase angle between 0° and 90°. The loss factor (tanδ) was calculated as follows:

$$tan\delta = \frac{G'}{G''} \quad \text{(VII)}$$

Rotational tests evaluated the blend's structural and compositional behavior. Newton's law was used to describe the viscous behavior of the blends:

$$\tau = \eta\dot{\gamma}^n \quad \text{(VIII)}$$

where τ denotes the shear stress (Pa), η represents the flow consistency index (Pa·s^n), $\dot{\gamma}$ is the shear rate (s^{-1}), and n is the power-law exponent characterizing the material's flow behavior.

2.9. Fourier- transform infrared spectroscopy

Fourier- transform infrared (FTIR) spectroscopy, operated in attenuated total reflection (ATR) mode using a Vertex 70 spectrometer (Bruker Optik GmbH, Germany) equipped with a platinum ATR accessory and diamond crystal, was employed to verify the incorporation of BC in the printed filaments. Spectral data were collected over the 400–4000 cm^{-1} range at a resolution of 1 cm^{-1} for material characterization.

2.10. X- ray diffraction

The X-ray diffractometer (XRD) X'Pert Pro PANalytical (Malvern Panalytical, UK), equipped with Cu/Kα radiation (wavelength: 0.154 nm), was used to confirm the crystalline structure by scanning in the 2θ range of 0–50° at a scanning speed of 0.1 °/min . The average crystallite size (D) was determined using the Scherrer equation:

$$D = \frac{K\lambda}{Bcoscos\,\theta} \quad \text{(IX)}$$

where λ is the wavelength (1.54 Å), B is the full width at half maximum, θ is the Bragg's diffraction angle, and K is a constant of 0.94.

2.11. Differential scanning calorimetry

Differential scanning calorimetry (DSC) tests were performed using a TA Q100 instrument (TA Instruments, USA) under a nitrogen atmosphere with a flow rate of 50 mL/min and a heat –cool –heat procedure. The samples (n = 3) were initially heated from −90 to 280 °C at a rate of 20 °C/min, then rapidly cooled back to −90 °C at the same rate, followed by a second heating cycle to 280 °C at a reduced rate of 10 °C/min. The melting temperature (T_m), crystallization temperature (T_c), melting enthalpy (ΔH_m), crystallization enthalpy (ΔH_{mc}), and glass transition temperature (T_g) were analyzed from the DSC graphs using Universal Analysis Software (TA Instruments, USA). Crystallinity (χ_c) was calculated using the following equation:

$$\chi_c(\%) = \left(\frac{\Delta H_m - \Delta H_p}{\Delta H_m}\right) \times 100 \quad \text{(X)}$$

where ΔH_m is the melting enthalpy and ΔH_p = 8 J/g is the melting enthalpy of PETG with complete crystallization.[30]

2.12. Mechanical analysis

Uniaxial static compression testing was performed using an Instron 3344 system (Instron, USA). The scaffolds were sectioned into small cubic samples with approximate dimensions of 4.5 × 4.5 × 5 mm (length × width × height). For each material concentration, samples (n = 4) were tested using a 500 N load cell and a strain rate of 0.5 mm/min. Compressive modulus was obtained from the linear region

of the stress–strain curve, while the yield strength was determined by the intersection of the 0.2% strain offset line with the stress–strain curve .

2.13. *In vitro* studies

2.13.1. Cell culture

Scaffolds ($n = 5$) were cut into small cubes of approximately 6.5 × 6.5 × 2.5 mm (length × width × height), sterilized using ethanol/deionized water (80:20) for 4 h, and washed twice with PBS. The scaffolds were placed into 24-well plates and left to dry under a cell culture hood for 24 h. Human adipose-derived stem cells (hADSCs) (ThermoFisher Scientific, UK) (passage 6) were cultured in T-75 cell culture flasks using MesenPRO RS cell culture medium containing 2 vol% growth supplement, 1 vol% penicillin/streptomycin, and 1 vol% glutamine. The flasks were placed inside an incubator (37 °C, 5% CO_2, and 95% humidity) for 2 days to achieve 92 –95% cell confluency. Cells were then seeded onto each scaffold (in dry state) at a density of approximately 62,500 cells/μL, using 0.8 μL cell suspension (approximately 50,000 cells). The culture medium was replaced every 2 days.

2.13.2. Cell metabolic activity

On days 1, 3, 7, and 14, the Resazurin assay (Alamar Blue) was used to assess metabolic activity and seeding of the cells. Samples were incubated for 4 h by adding 0.01% (v/v) of Alamar Blue (70 μL) in cell culture media (0.7 mL). The absorbance of the sample solution (0.2 mL) was read using the Infinite 200 microplate reader (Tecan, Switzerland) at a wavelength of 570 nm.

2.13.3. Cell proliferation analysis

The MTT (3-(4,5-dimethylthiazol-2-yl)-2, 5-diphenyltetrazolium bromide) assay kit was used to evaluate cell proliferation on different materials over a 14-day culture period. A 50 wt% MTT reagent solution was mixed with an equal volume of 50 wt% DMEM (Dulbecco's Modified Eagle Medium) and applied to each sample (0.5 mL). The samples were incubated in the dark, covered with aluminum foil, for 3 h . After incubation, the reagent was removed without washing with PBS, and 0.75 mL of a 1:1:3 MTT solvent was added to each sample, which was again covered with aluminum foil. The plates were then gently stirred for 15 min at room temperature (25 °C). The absorbance of the scaffold solutions (0.2 mL) was measured at 590 nm using the Infinite 200 microplate reader (Tecan, Switzerland).

2.13.4. Cell differentiation analysis

The ALP Assay Kit was employed to assess the differentiation potential of the materials over a 14-day differentiation period. Cells were seeded on the scaffolds and allowed to proliferate for 7 days. Thereafter, the proliferation medium was replaced with the osteogenesis differentiation medium. Scaffolds were washed twice with 1×ALP assay buffer, followed by the addition of 1×ALP assay buffer containing 0.2 vol% Triton X-100. Following this, the samples were agitated using a vortex mixer for 1 min, ultrasonicated for 3 min, and subsequently subjected to repeated freez e–thawing at −80 °C. Samples underwent centrifugation at 2500 × g for 10 min at 4 °C. The collected supernatant was combined with a para-nitrophenyl phosphate substrate solution and incubated at room temperature (25 °C) for 1 h. The absorbance of the scaffold solution (0.2 mL) was measured at 405 nm using the Infinite 200 microplate reader (Tecan, Switzerland). ALP activity was normalized to the total protein concentration determined by the BCA assay, with results calculated based on a standard curve.

2.13.5. Immunofluorescence analysis

Confocal immunofluorescence microscopy was used to evaluate cell proliferation, bridging, and morphology. Confocal images were taken using a Leica TCS SP8 Confocal Microscope (Leica Company, Germany). Cells on day 14 were fixed on the scaffolds using formaldehyde (37%) for 30 min and rinsed thoroughly three times with PBS . Cells were permeabilized with Triton-X 100 (0.1% in PBS) solution for 3 min and blocked with 0.5% fetal bovine serum for 1 h. Scaffolds were incubated with 1:400 Alexa Fluor 594 Phalloidin solution for 45 min and subsequently with 300 nM DAPI solution for 5 min. After each step, the scaffolds were rinsed three times with PBS. Confocal images were analyzed using Image J.

2.13.6. Scanning electron microscopy

SEM was used to assess cell proliferation and expansion on the top and cross-section of the scaffolds using the dry-freezing technique. Scaffolds on day 14 were fixed using formaldehyde (37%) for 30 min and rinsed thoroughly three times. Thereafter, ethanol and deionized water mixtures (v/v) at different ratios (50:50, 60:40, 70:30, 80:20, 90:10, 100:0) were used, followed by a 50:50 (v/v) solution of HMDS and ethanol; e ach step lasted 15 min. Finally, 100% HMDS was applied and left to evaporate overnight under the cell culture hood . The scaffolds were then coated with a 10 nm-thick layer of platinum/palladium (80:20).

2.14. Statistical analysis

Each methodology section includes the number of scaffolds and materials (n) used for the tests. The results were presented as mean ± standard deviation . Statistical analysis was conducted using one-way analysis of variance with Tukey post hoc test using Prism 10 software (GraphPad Software Inc., USA). Significant differences

were considered at $^{*}p < 0.05$, $^{**}p < 0.01$, $^{***}p < 0.001$, and $^{****}p < 0.0001$. Data analysis was conducted using Prism 10 software and Origin 2021 (Origin Lab Corporation, USA).

3. Results

3.1. Morphological and surface characterization properties of fabricated filaments and 3D-printed scaffolds

Filaments composed of PETG and PETG/BC, with a constant diameter of 1.75 mm, were successfully produced. PETG-based scaffolds with a uniform structure were then fabricated using material extrusion 3D printing (Figure 1a and b). The 3D-printed scaffolds exhibit similar morphological properties (pore size, filament width, layer thickness, and porosity) to the designed parameters (Table S2). For all material compositions, the scaffolds present uniform circular filaments during the extrusion process, indicating a constant printing procedure. Top and cross-sectional analyses revealed that PETG/BC filaments have a rougher surface with visible surface micro-pores, and the roughness increases with increasing BC concentration. In contrast, PETG-only scaffolds exhibit a smooth surface (Figure 1a and b; Table S3).

The WCA of the scaffolds at 0 s ranges from ~106° to ~97°, indicating that all scaffolds are hydrophobic. However, the increase of BC concentration decreases the hydrophobicity of the scaffolds (Figure 2a and b; Table 1). After 1 min, the hydrophobicity of the scaffolds significantly decreases (94.1° for PETG/BC [90/10 wt%], 90.77° for PETG/BC [85/15 wt%], and 84° for PETG/BC [80/20 wt%]) (Figure 2a; Table 1). In contrast, PETG-scaffolds maintain a slightly higher hydrophobicity (~95°). As observed for both time points, the highest WCA values were obtained for PETG/BC (80/20 wt%) scaffolds, while the lowest values were observed for PETG-only scaffolds.

Figure 2d–g displays the AFM topographical maps taken over a 1 μm scan area for all scaffolds, while Figure 2h–k features the corresponding maps taken over a 10 μm area. Figure 2c presents the Root Mean Square (RMS) Roughness (Rq) values, which indicate the deviation from the average roughness (Ra). The topographical maps and roughness measurements indicate that PETG scaffolds exhibit higher roughness at increasing BC concentration, as evidenced by the increase in amplitude between peaks and valleys . BC content up to 10 wt% appears to have minimal impact on surface characteristics, whereas concentrations of 10 –15 wt% and 15–20 wt% result in notable changes in surface texture and roughness.

3.2. Rheological analysis

Rheology tests were conducted to investigate the printability of the materials fabricated using fused deposition modeling (FDM) at three different temperatures (190, 200, and 210 °C) (Figure 3a–c). Oscillation results revealed that the incorporation of BC enhances storage and loss moduli, indicating increased energy stored within the polymer (Figure 3a). However, at 200 °C, PETG/BC (85/15 wt %) and PETG/BC (80/20 wt%) exhibited a decrease in both moduli compared to pure PETG. Moreover, results indicated that both moduli decreased with increas ing temperature, reflecting a reduction in melt stiffness due to increased thermal energy that promotes polymer chain mobility and reduces resistance to deformation. Conversely, the increase in frequency increases both storage and loss moduli for all material blends, indicating enhanced viscoelasticity and a transition from liquid-like (viscous) to more solid-like (elastic) behavior under faster deformation . However, the storage modulus remains lower compared to the loss modulus, confirming the viscoelastic behavior of the blends. The loss factor (tanδ) decreases as the frequency increases beyond 0.1 Hz. Similarly, at frequencies above 0.1 Hz, an increase in temperature displays a similar pattern. This suggests that the materials behave more elastically, making them easier to print (Figure 3b). The incorporation of BC did not significantly impact tanδ, suggesting that BC does not significantly alter the balance between elastic and viscous responses during deformation. The rotational results revealed that viscosity increases with higher BC content at low shear rates (Figure 3c). However, as the shear rate increases, the viscosity decreases, indicating a shear-thinning behavior for all material blends. This can be explained by the high melting point of BC (> 330 °C) and the interconnection between the BC particles and the polymer. Moreover, the increase in temperature results in a decrease in dynamic viscosity, likely due to increased polymer chain mobility, thereby enhancing flow behavior and the printability of the materials.

3.3. Physical properties of the 3D-printed scaffolds

The PETG and PETG/BC scaffolds exhibit a stress–strain curve characterized by an initial elastic region followed by plastic deformation, where the stress surpasses the yield point (Figure 4a). Results indicate an increase in plastic deformation with the incorporation of BC particles, with yield stress values increasing from 7.8 MPa for pure PETG to 9.3 MPa for PETG/BC (90/10 wt%), 11.7 MPa for PETG/BC (85/15 wt%), and 12.5 MPa for PETG/BC (80/20 wt%), reflecting an increase in stiffness (Figure 4a). For all materials, the plastic region features a smooth curve, indicating that PETG and PETG/BC are ductile materials. In addition, the 0.2 offset yield strength and compression increase with increasing BC concentration from ~9.5 to ~12 MPa and ~205 to ~230 MPa, respectively (Figure 4b and c). Overall, PETG/BC (80/20 wt%) exhibited the

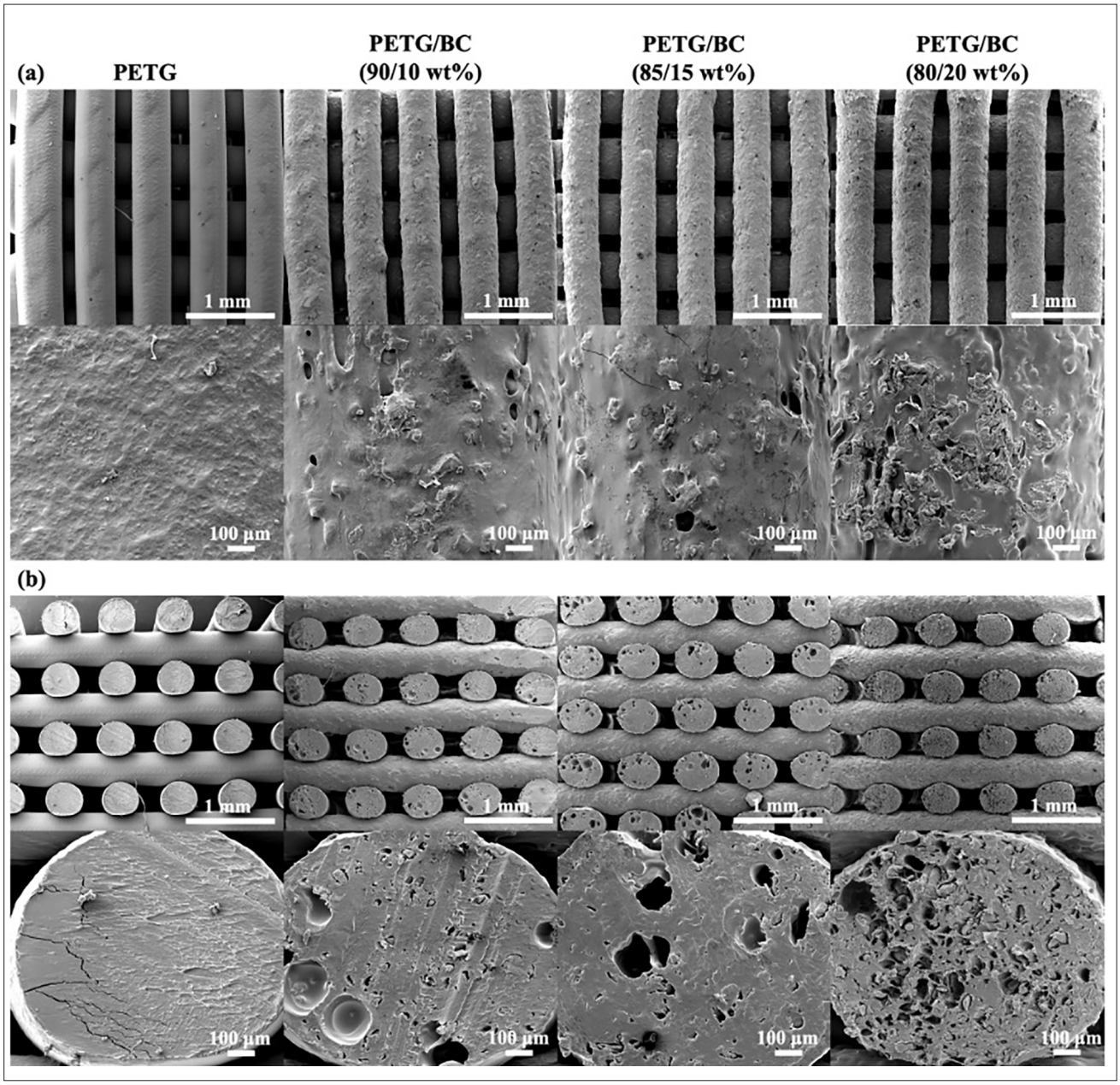

Figure 1. Scanning electron microscopy images of (a) top view and (b) cross-sectional view of PETG, PETG /BC (90/10 wt%), PETG/BC (85/15 wt%), and PETG/BC (80/20 wt%). Scale bars: 1 mm (a and b, top); 100 µm (a and b, bottom). Abbreviations: BC: bacterial cellulose; PETG: polyethylene terephthalate glycol.

highest compression (~230 MPa) properties compared to the other material blends.

3.4. Chemical properties of the 3D-printed scaffolds

The effect of BC as a potential nucleation agent for crystallization was investigated using DSC to identif y the thermal cycling effect on the materials' properties.[30] The results (Figure 5a–e; Table 2) indicate that during the first heating cycle, the incorporation of BC increases the glass transition temperature (T_g), melting temperature (T_m), enthalpy (ΔH), and crystallinity (χ_c). In contrast, an opposite

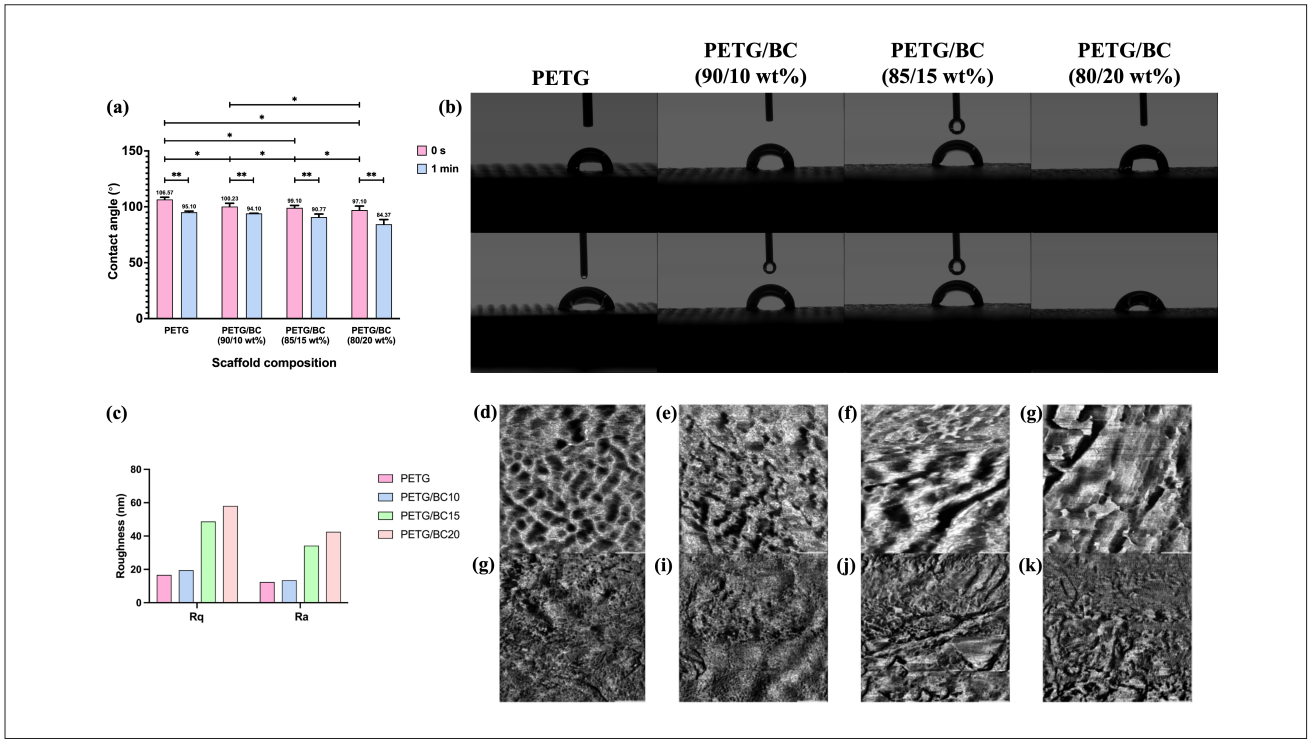

Figure 2. Scaffold morphology and roughness. (a) Water contact angle (WCA) results at 0 s and 1 min. (b) WCA images of PETG and PETG/BC scaffolds. (c) Rq and Ra roughness values measured using atomic force microscopy (AFM) images. (d–k) AFM images taken at 1 μ m scale for PETG (d), PETG/BC (90/10 wt%) (e), PETG/BC15 (85/15 wt%) (f), and PETG/ BC (80/20 wt%) (g), as well as at 10 (m scale for PETG (h), PETG/ BC (90/10 wt%) (i), PETG/ BC (85/15 wt%) (j), and PETG/ BC (80/20 wt%) (k). *$p < 0.05$; **$p < 0.01$; $n = 4$. Scale bars: 1 μm (d–g); 1 μm (h–k). Abbreviations: BC: bacterial cellulose; PETG: polyethylene terephthalate glycol.

Table 1. Water contact angle results of printed scaffolds at 0 s and 1 min

Materials	Water contact angle (°)	
	0 s	1 min
PETG	106.57 ± 1.99	95.1 ± 1.03
PETG/BC (90/10 wt%)	100.23 ± 2.96	94.1 ± 0.1
PETG/BC (85/15 wt%)	99.1 ± 2.1	90.77 ± 2.78
PETG/BC (80/20 wt%)	97.1 ± 3.6	84.37 ± 4.24

Abbreviations: BC: bacterial cellulose; PETG: polyethylene terephthalate glycol.

effect was observed during the second heating cycle (Figure 5a and b). During the heat –cool –heat process, the ΔH initially increased from 17.02 J/g for pure PETG to 17.92 J/g for PETG/BC (90/10 wt%), 18.49 J/g for PETG/BC (85/15 wt%), and 20.91 J/g for PETG/BC (80/20 wt %) in the first heating cycle; decreased to 15.26 J/g for pure PETG, 11.32 J/g for PETG/BC (90/10 wt%), 12.48 J/g for PETG/ BC (85/15 wt%), and 13.11 J/g for PETG/BC (80/20 wt%) during the cooling phase; and increased again to 16.98 J/g for pure PETG, 16.46 J/g for PETG/BC (90/10 wt%), 15.22 J/g for PETG/BC (85/15 wt%), and 13.72 J/g for PETG/ BC (80/20 wt%) in the second heating phase (Table 2). Moreover, χ_c significantly decreases from the first heating phase (52.92% for pure PETG, 53.09% for PETG/BC [90/10 wt%], 54.86% J/g for PETG/BC [85/15 wt%], and 59.48% for PETG/BC [80/20 wt%]) to the second heating phase (50.35% for pure PETG, 48.67% for PETG/BC [90/10 wt%], 45.08% J/g for PETG/BC [85/15 wt%], and 40.69% for PETG/BC [80/20 wt%]), suggesting limited rearrangement of the polymeric chains. However, during the second heating phase, BC has a negative effect on the crystallinity, indicating poor interconnectivity between BC and PETG after the recrystallisation process. The T_m results did not display significant differences with the incorporation of BC for both the first heating cycle (~76–78 °C) and second heating cycle (~76–78 °C), indicating that the incorporation

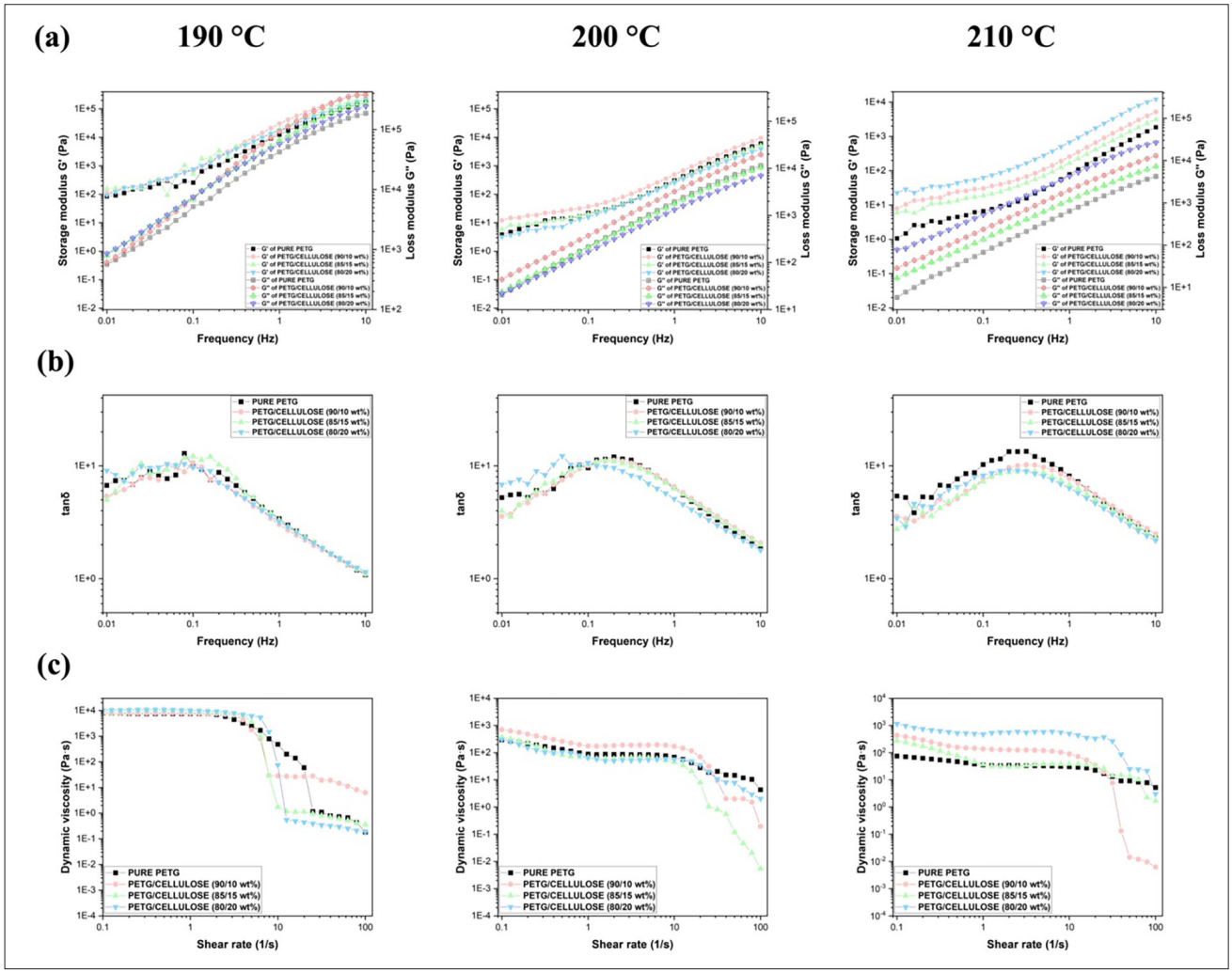

Figure 3. Rheological properties of material blends at different temperatures (190, 200, and 210 °C). (a) Storage and loss moduli results. (b) Loss factor (tanδ) results. (c) Dynamic viscosity results. Abbreviations: BC: bacterial cellulose; PETG: polyethylene terephthalate glycol.

of BC does not affect the energy required for the system to break down the crystal microstructure. The incorporation of BC did not affect the T_c of the polymer (~76–79 °C), indicating that the recrystallisation process and polymer chain mobility are not affected during the transition from the molten to solid state . Similarly, the T_m of the materials remained nearly constant (Figure 5c). For all material blends, the T_g results did not present any differences with the increase of BC content for both the first heating cycle (~68 °C) and the second heating cycle (~65 °C). However, the slight decrease in T_g during the second heating cycle suggests that neither the incorporation of BC, the printing process, nor reheating the materials affects the amorphous region of PETG (Figure 5d and e).

The FTIR analysis verified the successful incorporation of both PETG and BC in the scaffold matrix (Figure 6a). The similarity in the peaks confirms that the thermal blending method is a physical phenomenon that does not change the PETG chemical structure. However, there are some minor shifts with the incorporation of BC, which can be attributed to the interactions between the chemical groups. PETG peaks at 725 and 958 cm^{-1} represent the out-of-plane C –H and cyclohexylene ring, respectively.[31] Peaks at 1240, 1451, and 1712 cm^{-1} are attributed to the C(O)–O stretching of the ester group, $–CH_2–$deformation band, and C=O ester groups.[32] Moreover, peaks found at 2850 and 2924 cm^{-1} are the asymmetric and symmetric aliphatic C–H stretching vibrations.[33] Additionally, BC peaks are found at 847 and 3347 cm^{-1}, depicting the β-1, 4-glycosidic bond vibration and the –OH stretching vibration. With the incorporation of BC, the 2924 cm^{-1} peak shifts to a lower wavenumber by 5 cm^{-1}.

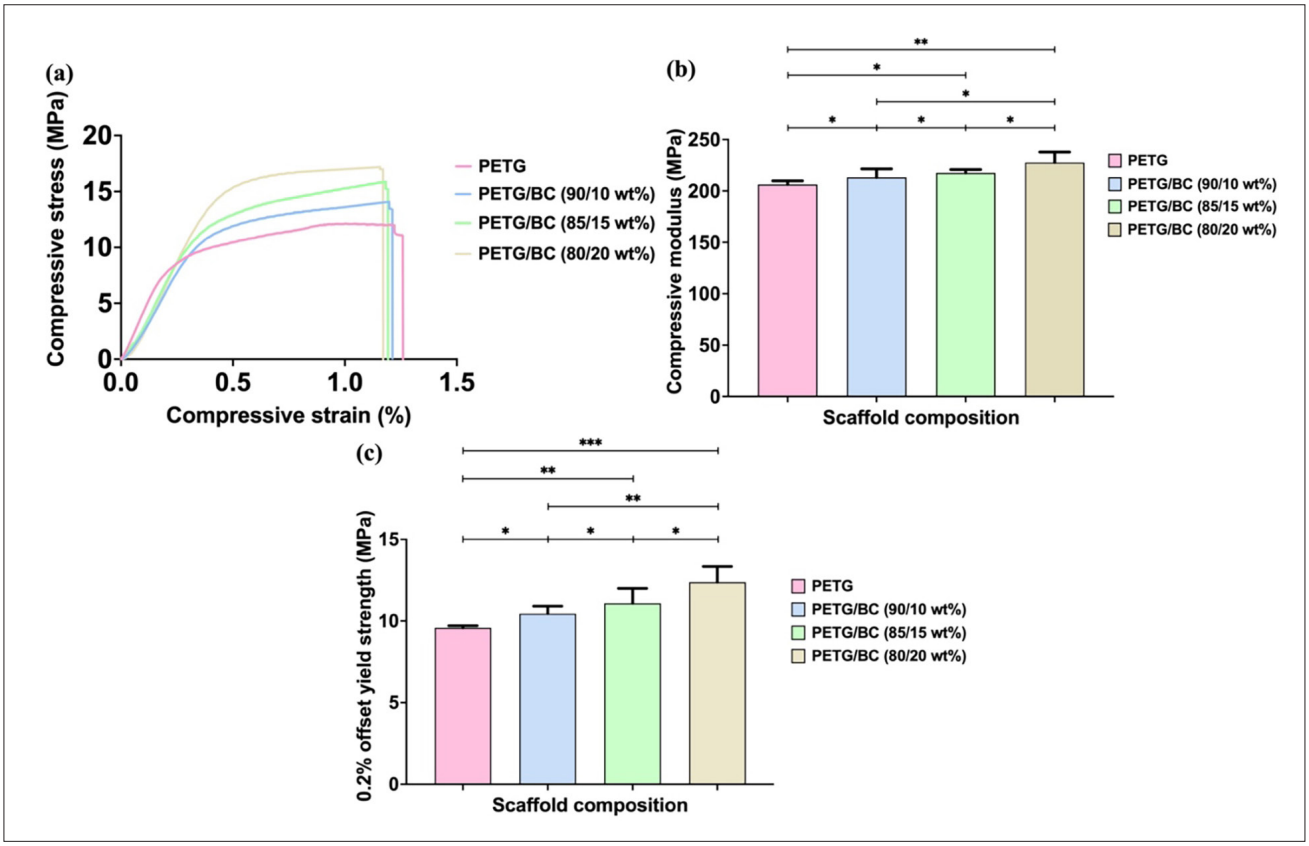

Figure 4. Mechanical properties of printed scaffolds: (a) compressive stress–strain curves, (b) compressive modulus results, and (c) 0.2% offset yield strength results . $^{*}p < 0.05$, $^{**}p < 0.01$, $^{***}p < 0.001$; $n = 4$. Abbreviations: BC: bacterial cellulose; PETG: polyethylene terephthalate glycol.

Figure 6b presents four spectra of PETG, PETG/ BC (90/10 wt%), PETG/ BC (85/15 wt%), and PETG/ BC (80/20 wt%). The spectra have the constituent peaks for PETG at 27.56°, 36.16°, 39.29°, 41.38°, and 44.16°.[34] With the incorporation of BC, three different phenomena can be identified: (i) broadening of the primary peak at 19.11°, (ii) the appearance of a new peak at 22.33°, and (iii) a shift of several peaks to ward lower angles.[35] These observations highlight the chemical and physical changes in the material due to BC incorporation. Additionally, the scaffolds' crystallinity and crystallite size were analyzed using the Scherrer method to study the effect of BC on the nucleation behavior. As displayed in Figure 6b and c, the increase in crystallinity and crystallite sizes can be attributed to the increase in BC content. Crystallinity increased by 10%, and the crystallite size increased from 29.48 to 32.64 nm as the BC content increased from 10 to 20 wt%.

These findings align with the thermal analysis, where DSC results displayed increased crystallinity and enthalpy with higher BC content (Table 2). Taken together, the FTIR, XRD, and DSC results confirm that BC acts as a physical reinforcement and nucleating agent within the PETG matrix, improving both the structural order and thermal behavior of the composite scaffolds.

3.5. *In vitro* properties of the 3D-printed scaffolds

hADSCs were seeded on the different scaffolds to assess cell attachment, proliferation, and differentiation. Cellular metabolic activity was assessed using the Alamar Blue assay. From day 3 to day 14, a progressive increase in cell metabolic activity was observed, suggesting active proliferation and spreading on the scaffolds. This activity may be linked to the minerals released during material degradation (Figure 7a). Moreover, BC incorporation increased cell metabolic activity, with the highest value (~16,000 AU) observed for PETG/BC (80/20 wt%) on day 14, implying that cell proliferation is positively affected by the presence of BC. In contrast, PETG-only scaffolds exhibited the lowest metabolic activity (~12,000 AU).

The MTT assay was used to quantify cell attachment and proliferation on the scaffolds (Figure 7b). The results were consistent with those from the Alamar Blue assay . On day 3, a high number of cells was observed across all the different material concentrations, with PETG/BC (90/10

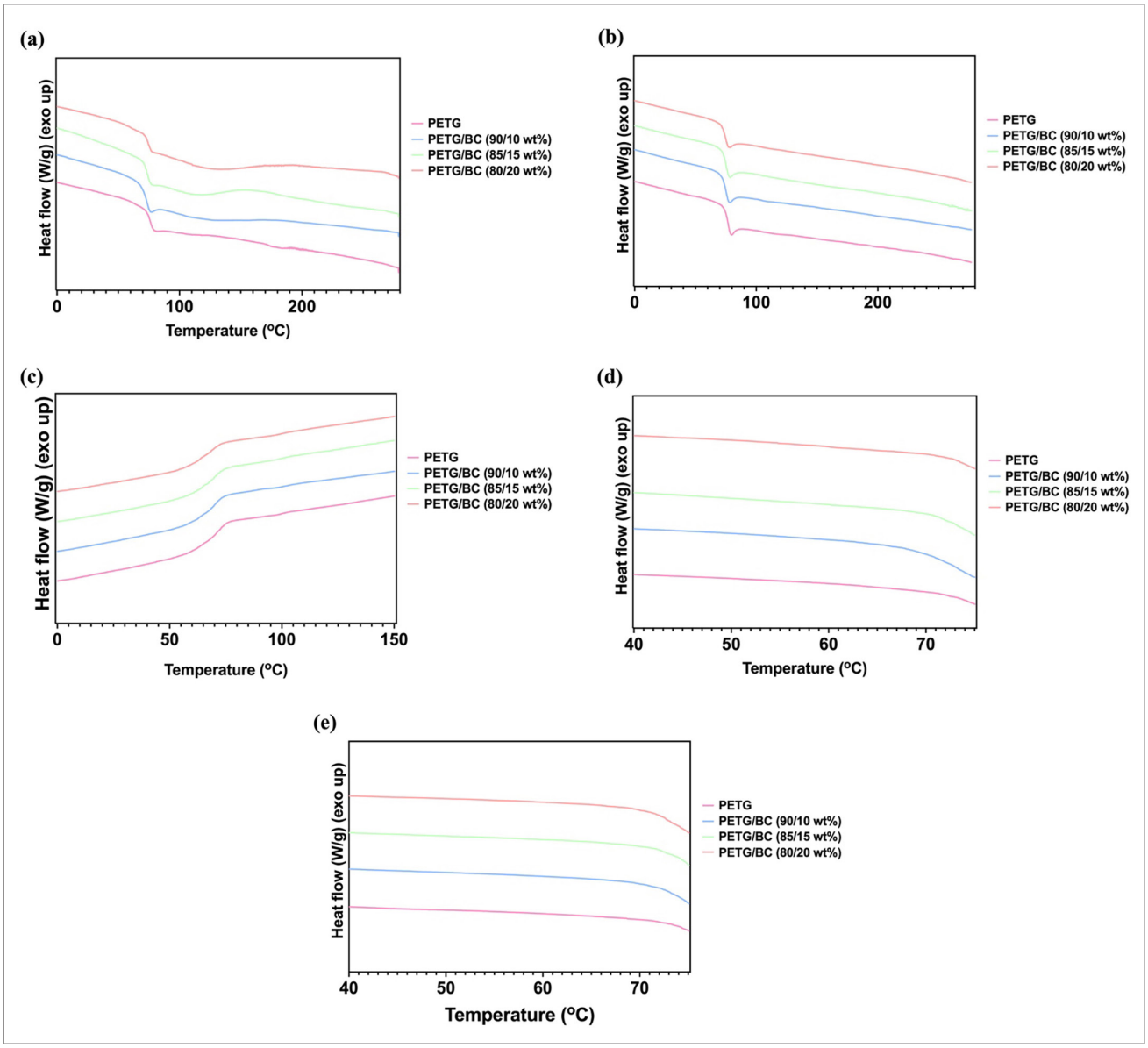

Figure 5. Differential scanning calorimetry (DSC) analysis: (a) first heating cycle; (b) second heating cycle; (c) cooling cycle; (d) glass transition temperature during the first heating cycle; and (e) glass transition temperature during the second heating cycle. Abbreviations: BC: bacterial cellulose; PETG: polyethylene terephthalate glycol.

wt%) presenting the highest number of cells (~53,000 cells) and PETG/BC (80/20 wt%) reporting the lowest number of cells (~43,000 cells). The lower number of cells in PETG/BC (80/20 wt%) is attributed to the smaller pore size and limited available space for cell growth and proliferation. On day 7, cell numbers increased but displayed a similar trend to day 3, ranging from ~132,000 cells for the PETG/BC (80/20 wt%) scaffold to ~142,000 cells for the PETG/BC (90/10 wt%) scaffold. By day 14, cell numbers continued to increase, with the PETG/BC (80/20 wt%) scaffold presenting the highest cell count (~204,000 cells), followed by the PETG/BC (85/15 wt%) scaffold (~179,000 cells) and the PETG/BC (90/10 wt%) scaffold (~177,000 cells). Pure PETG exhibited the lowest cell count (~164,000 cells). This trend is ascribed to the increased surface roughness of PETG/BC (80/20 wt%) scaffolds, which may facilitate better cell adhesion and growth.

The ALP assay was used to evaluate the osteogenic differentiation of cells across different BC concentrations

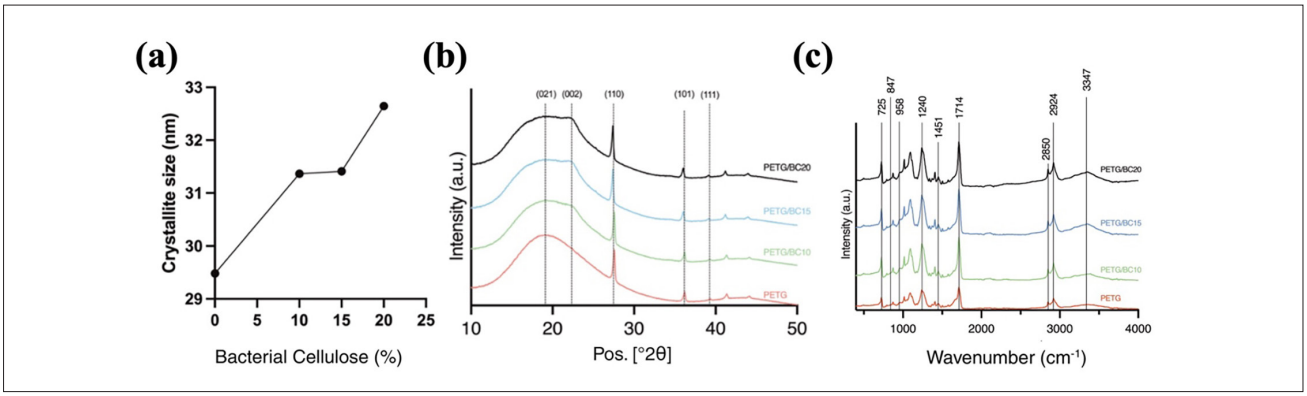

Figure 6. Physical characteristics of the printed scaffolds: (a) FTIR analysis; (b) XRD analysis of PETG and PETG/BC scaffolds; and (c) analysis of crystallite size. Abbreviations: BC, bacterial cellulose; PETG, polyethylene terephthalate glycol; FTIR, Fourier transform infrared spectroscopy; XRD, X-ray diffraction.

Table 2. Differential scanning calorimetry (DSC) results of the printed scaffolds

Cycle	Material	T_g (°C)	T_m (°C)	T_c (°C)	χ_c (%)
First heating	PETG	68.66 ± 0.07	78.86 ± 0.15	17.02 ± 0.1	52.91 ± 0.77
	PETG/BC (90/10 wt%)	68.45 ± 0.04	76.34 ± 0.08	17.92 ± 0.03	53.09 ± 0.95
	PETG/BC (85/15 wt%)	68.27 ± 0.01	76.46 ± 0.07	18.49 ± 0.05	54.86 ± 1.68
	PETG/ BC (80/20 wt%)	68.19 ± 0.08	77.39 ± 0.12	20.91 ± 0.09	59.48 ± 2.63
Cooling	PETG	–	75.72 ± 0.03	15.26 ± 0.06	45.15 ± 1.81
	PETG/BC (90/10 wt%)	–	73.95 ± 0.33	11.32 ± 0.03	35.55 ± 0.86
	PETG/BC (85/15 wt%)	–	74.01 ± 0.09	12.48 ± 0.01	36.98 ± 0.3
	PETG/BC (80/20 wt%)	–	73.08 ± 0.07	13.11 ± 0.07	39.12 ± 2.62
Second heating	PETG	66.23 ± 0.02	78.45 ± 0.21	16.98 ± 0.04	50.35 ± 1.46
	PETG/BC (90/10 wt%)	65.94 ± 0.02	76.72 ± 0.14	16.46 ± 0.07	48.67 ±2.16
	PETG/BC (85/15 wt%)	64.74 ± 0.03	76.44 ± 0.17	15.22 ± 0.01	45.08 ± 1.3
	PETG/BC (80/20 wt%)	64.44 ± 0.06	76.43 ± 0.22	13.72 ± 0.05	40.69 ± 1.7

Abbreviations: BC: bacterial cellulose; PETG: polyethylene terephthalate glycol.

(Figure 7c). A significant increase in ALP activity was observed from day 3 to day 14, indicating enhanced osteogenic differentiation of the hADSCs. On day 3, BC-containing scaffolds presented higher ALP activity compared to pure PETG scaffolds, though not statistically significant . By days 7 and 14, ALP activity increased with BC content, again without significant differences . Among the different scaffolds, PETG/BC (80/20 wt%) displayed the highest ALP activity, likely due to its high surface roughness, which better mimics natural bone.

SEM and confocal images confirmed that cells spread and filled the porous areas of the scaffolds, indicating no cytotoxicity (Figure 8a and b). Cell numbers and surface coverage increased with higher BC concentrations . Due to the dense cell population, DAPI staining produced overly bright signals, limiting confocal image clarity (Figure S1). Therefore, bright -field imaging was applied in Figure S1, highlighting cell bridging and proliferation between the porous areas, with an increased number of cells being observed at increas ing BC concentration.

4. Discussion

In this research, 3D-printed scaffolds were successfully fabricated using FDM, and their characteristics were studied. A twin-screw extruder was used to produce a homogeneous mixture of PETG and BC. In order to achieve a well-defined 3D printed structure, the influence of printing parameters and filler concentration on material properties was investigated. Among those parameters, the most critical are the extruding parameters and rheology characteristics of the materials.

The incorporation of BC increas ed the printing temperature and viscosity, corresponding to a decrease in

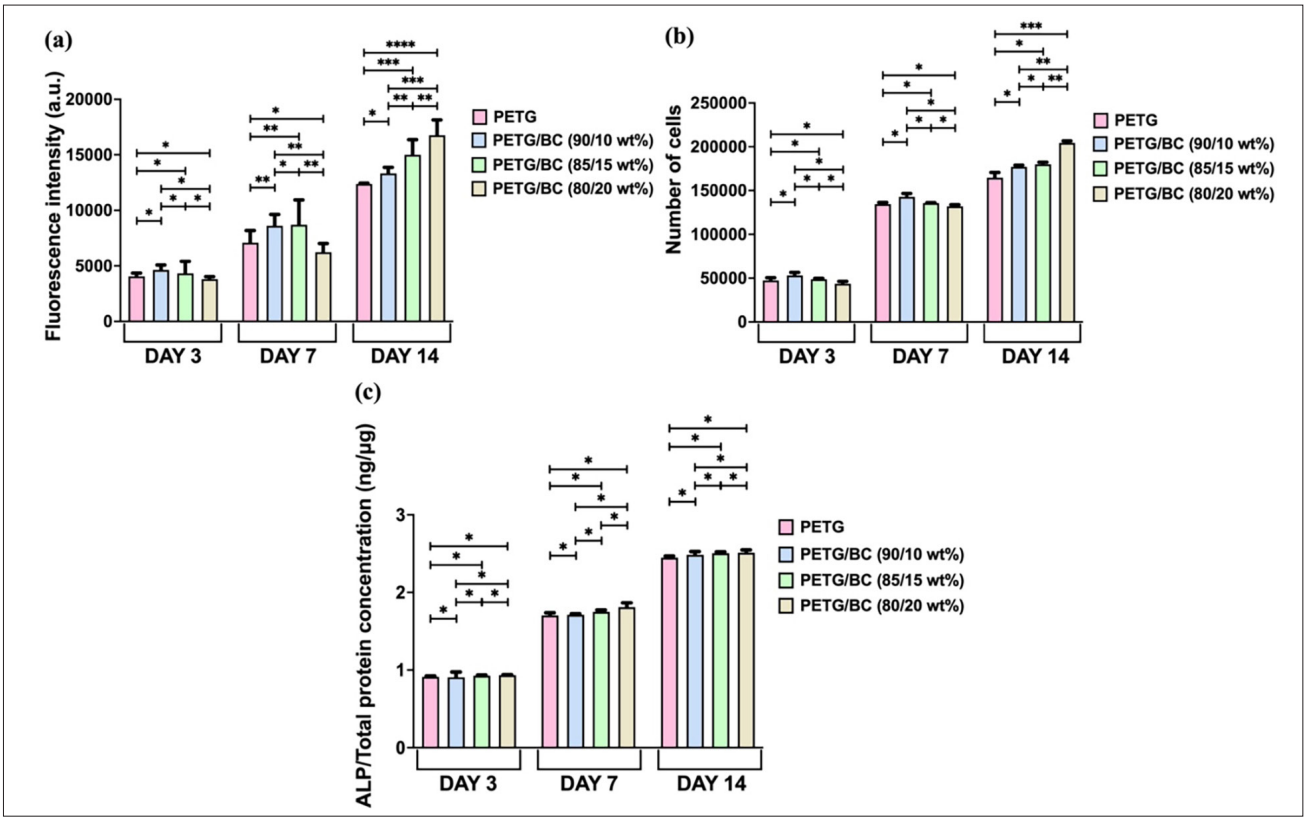

Figure 7. Biological characteristics of the printed scaffolds. (a) Metabolic activity of hADSCs assessed by Alamar Blue assay on days 3, 7, and 14. (b) Cell proliferation measured by MTT assay on days 3, 7, and 14. (c) Normalized ALP activity indicating osteogenic differentiation of hADSCs across different scaffold compositions on days 3, 7, and 14. $^{*}p < 0.05$, $^{**}p < 0.01$, $^{***}p < 0.001$, $^{****}p < 0.0001$; $n = 5$. Abbreviations: BC: bacterial cellulose; PETG: polyethylene terephthalate glycol.

polymer chain movement and flowability. Techawinyutham *et al.*[36] fabricated PETG with recycled high-density polyethylene and low-density polyethylene at various concentrations (0–100 wt%) using a compression molding process, and revealed that decreas ing the PETG content led to decreases in storage modulus, loss modulus, and viscosity. A similar trend was observed by Bhandari *et al.*,[37] who observed that increasing carbon fiber concentration in PETG, using an extrusion-based 3D printing process, led to reductions in storage modulus, loss modulus, and viscosity. Therefore, the results reported in this paper are consistent with previous studies, indicating that BC incorporation in the blend enhances viscosity.

The FDM 3D-printed scaffolds exhibited pore sizes and filament widths consistent with the design specifications, with no direct effect from BC incorporation. Morphological analysis confirmed the presence of micro por es and increased surface roughness, both of which were intensified with higher BC content. The formation of micro por es and increased surface roughness can be attributed to the high temperatures used during filament fabrication (>190 °C) and rapid solidification.[38] Based on *in vitro* and *in vivo* assessments, the formation of intrafiber pores on scaffolds promoted better cell adhesion, proliferation, growth, and differentiation compared to scaffolds with smooth surfaces and no intrafiber pores.[39] This was confirmed by the biological results in this study, where increased fiber microporosity, and thus surface area, promoted greater cell adhesion, proliferation, and growth. While microporosity is associated with reduced mechanical properties due to crack formation and structure failure,[40] the scaffolds in this study maintained mechanical integrity, likely due to increase d crystallinity.[41]

Wettability analysis revealed that increas ing BC content reduced WCA, enhancing scaffold hydrophilicity due to the hydrophilicity of BC.[42] Scaffold morphology—governed by surface roughness and microporosity—played a key role in this behavior . Higher BC concentration led to rougher surfaces and more micro pores, which improved water absorption and further decreased WCA.[43] According

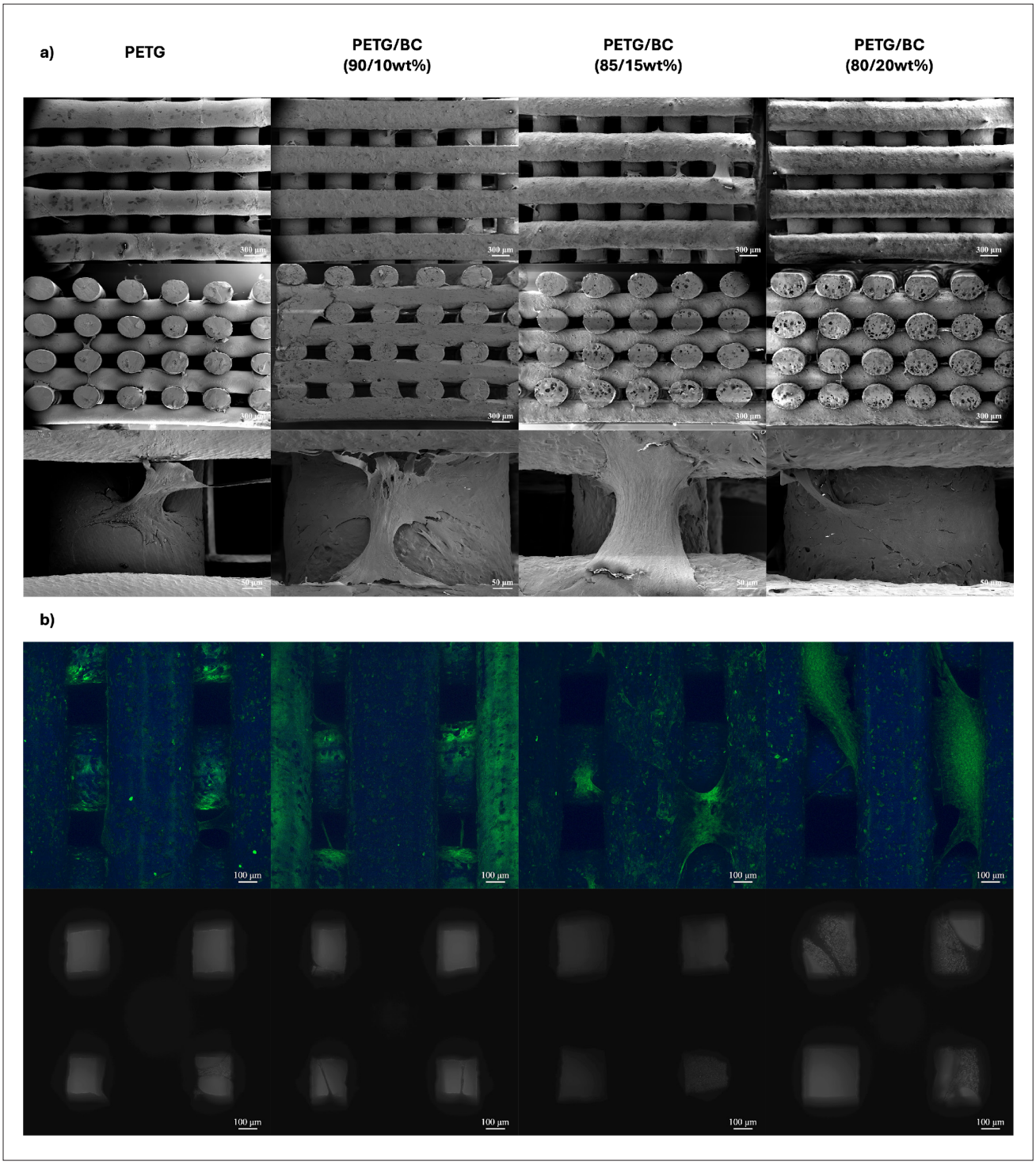

Figure 8. Cell attachment and proliferation on scaffold surfaces on day 14. (a) SEM images of the top and cross-sectional views of cell-seeded scaffolds . (b) Confocal and bright-field images (top and cross-sectional views) of cell-seeded scaffolds . Scale bars: 300 µm (a, top and middle); 100 µm (b); 50 µm (a, bottom). Abbreviations: BC: bacterial cellulose; PETG: polyethylene terephthalate glycol; SEM: scanning electron microscopy.

to previous studies, increased wettability, surface roughness, and microporosity correlate with improved cell adhesion and tissue repair, indicating enhanced bioactivity with BC incorporation.[44]

The AFM topographical maps of PETG-based scaffolds highlight significant changes in surface morphology and roughness with increasing BC content. Pure PETG exhibited a relatively smooth surface with minor variations between peaks and valleys. At 10 wt% BC, a slight increase in overall roughness is observed, while 15 wt % BC exhibited more defined valleys and peaks, reflected in elevated Rq and Ra values (Figure 1g and k). At 20 wt% BC, the surface transitions to larger, planar peaks, indicating a significant morphological shift. These changes mimic the natural roughness of bone tissue, enhancing surface area and promoting cell attachment and growth, as supported by the biological results .

The DSC analysis revealed an increase in crystallinity and enthalpy with the incorporation of BC, while the T_g remained largely unchanged. These parameters are critical for influencing the mechanical and biological properties of the materials.[45] As PETG is predominantly amorphous (35–40% crystallinity), the incorporation of crystalline BC (60–80% crystallinity) serves as a nucleating agent, enhancing crystallinity through increased nucleation site formation and increased chain mobility.[46] The observed rise in enthalpy corresponds with increased crystallinity, reflecting the greater energy exchange during thermal cycling.[47] The unchanged T_g indicates that the amorphous nature of the blend remains dominant.[48]

The XRD analysis was used to evaluate the structure of PETG/BC scaffolds and the effect of BC concentration on crystallite sizes, which is key in improving the mechanical properties of bone tissue scaffolds to match bone tissue. As BC concentration increased, crystallite size generally grew, aligning with improvements in tensile strength. However, between 10–15 wt% BC, crystallite size remained relatively constant despite a marked increase in compressive strength. This suggests that crystallite growth primarily supports tensile properties, while compressive strength may be more affected by factors like voids or microstructural defects.

The FTIR results displayed a pronounced –OH peak at 3347 cm^{-1}, resembling the characteristic fingerprint of collagen in the 2750–3500 cm^{-1} range.[49] This is attributed to the hydrogen bonds present in both collagen and cellulose structures. Incorporating cellulose into synthetic polyesters like PETG enables the formation of strong hydrogen bonds akin to those in bone collagen,[50] which likely contributes to the enhanced mechanobiological performance observed with increasing BC content. FTIR analysis suggests that the optimal composition is PETG/BC at 80/20 wt%.

The chemical and morphological characteristics of the scaffolds significantly influence their mechanical properties. Compression tests revealed that increas ing BC concentration enhanced mechanical properties. Key parameters, such as porosity, pore size, and filament deposition, strongly impact the mechanical properties of the scaffolds.[3] Studies have reported that increas ing the porosity and pore size decreases the compressive modulus.[11] The 0/90° filament deposition has demonstrated much higher compression properties compared to 0/30° and 0/45° due to better connectivity between the pores and reduced surface density.[51] Yao and Chen[52] observed that the increased surface roughness also contributed to better mechanical properties by enlarging the contact area between fibers and matrix. Additionally, crystallinity and crystallite size directly impact the mechanical behavior of materials. Shuai *et al.*[53] produced scaffolds using poly(3-hydroxybutyrate-co-3-hydroxyvalerate) (PHBV) reinforced with zinc oxide (1, 3, and 5 wt%), which enhanced the mechanical properties of PHBV due to ordered stacking of polymer chains. The same trend was observed for poly-L- lactic acid (PLLA) scaffolds reinforced with carbon nanotubes (CNTs) (0.25, 0.5, and 1 wt%), where CNTs increase the crystallization of PLLA, leading to enhanced compressive modulus.[54] Huang *et al.*[55] also reported enhanced mechanical properties and increased crystallite size using PCL and β-tricalcium phosphate (20 and 40 wt%), validating the correlation between crystallite size and mechanical characteristics .

For bone tissue applications, scaffold biocompatibility and bioactivity are critical, alongside morphology, crystallinity, crystallite size, and mechanical properties of the scaffolds. Increas ing BC concentration enhanced cell attachment, proliferation, and differentiation, likely due to the release of bioactive elements, minerals, and increased oxygen availability.[56] The rougher surfaces and micropores introduced by BC enhanced scaffold hydrophilicity, supporting better cell interactions.[39] BC also increased crystallinity and crystallite size, enhancing mechanical properties and roughness of the scaffolds, which promote cell attachment and proliferation.[57] Scaffolds should be able to withstand high loads and provide mechanical properties similar to bone. Cell adhesion, proliferation, and differentiation rely on the cell's ability to sense and respond to mechanical cues at the nanoscale and microscale. Cells detect the density and stiffness of the material they attach to (mechanosensitivity) and convert this information into biochemical signals, leading to changes inside the cell.[58] Moreover, studies have reported that cell adhesion is

strongly dependent on the cytoskeleton, which is affected by the nanotopographical features of the material's surface, leading to the cell differentiation into bone or muscle tissue. Therefore, the incorporation of BC (and higher BC concentrations) significantly enhances the mechanical characteristics of the scaffolds, comparable to or exceeding those of trabecular bones (14–1 100 MPa), indicating an increase in bioactivity.[59,60]

This study focused on the effect of BC incorporation on the mechanical and biological behavior of PETG for bone tissue applications. While pure PETG demonstrated substantial mechanical and biological properties suitable for load-bearing applications and cell attachment and proliferation, the incorporation of BC significantly enhanced these properties . Among all blends, PETG/BC (80/20 wt%) exhibited the most favorable mechanical and biological properties .

5. Conclusion

In this study, PETG and PETG/BC scaffolds (0, 15, and 20 wt% BC) were successfully fabricated using the FDM additive manufacturing process. The incorporation of BC resulted in the formation of micro porous regions and increased surface roughness, enhancing scaffold morphology while maintaining consistent geometry and printability. Moreover, the presence of BC improved scaffold wettability, with WCA measurements indicating increased hydrophilicity at higher BC content. These morphological and surface modifications contributed to improved biological responses.

Chemical and thermal analyses confirmed the successful integration of BC into the PETG matrix. Higher BC content led to increased crystallinity and crystallite size, which positively influenced the scaffold's mechanical properties. All material blends exhibited shear-thinning behavior, making them suitable for FDM processing. Mechanical testing revealed that compressive modulus and yield strength increased with BC incorporation, with PETG/BC (80/20 wt%) demonstrating the highest mechanical performance.

Biological assays indicated that the PETG/BC scaffolds supported hADSCs attachment, proliferation, and osteogenic differentiation without signs of cytotoxicity. Increased BC content correlated with higher metabolic activity and ALP expression, suggesting improved bioactivity. Among all tested compositions, the PETG/BC (80/20 wt%) scaffold exhibited the most favorable combination of morphological, mechanical, and biological properties, indicating its strong potential for bone TE applications.

Acknowledgments

The authors would like to thank the University of Manchester, UK Research and Innovation (UKRI), Engineering and Physical Sciences Research Council (EPSRC), Henry Royce Institute for Advanced Materials, Nanyang Technological University (NTU), and Singapore Centre for 3D Printing (SC3DP) for their support and facilities.

Funding

This project was partially supported by the University of Manchester and UKRI through EPSRC (grant number: EP/V011766/1). Additionally, this work was also supported by the Henry Royce Institute for Advanced Materials (grant number: EP/S019367/1).

Conflict of interest

Paulo J.D.S. Bartolo is an Editorial Board Member of the journal, but was not in any way involved in the editorial and peer-review process conducted for this paper, directly or indirectly. Other authors declare they have no competing interests.

Author contributions

Conceptualization: Evangelos Daskalakis, Mohamed H. Hassan, Abdalla M. Omar, Paulo J.D.S. Bartolo

Data curation: Evangelos Daskalakis, Mohamed H. Hassan, Abdalla M. Omar, Maria Kapousidou, Dino Freitas, Mehmet Cagirici, Alexandra Lanot

Formal analysis: Evangelos Daskalakis, Mohamed H. Hassan, Abdalla M. Omar

Funding acquisition: Paulo J.D.S. Bartolo

Investigation: Evangelos Daskalakis, Mohamed H. Hassan, Abdalla M. Omar

Methodology: Evangelos Daskalakis, Mohamed H. Hassan, Abdalla M. Omar, Maria Kapousidou, Alexandra Lanot

Project administration: Evangelos Daskalakis, Mohamed, H. Hassan, Abdalla M. Omar, Paulo J.D.S. Bartolo

Resources: Evangelos Daskalakis, Mohamed H. Hassan, Abdalla M. Omar, Maria Kapousidou, Dino Freitas, Mehmet Cagirici

Software: Evangelos Daskalakis, Mohamed H. Hassan, Abdalla M. Omar, Maria Kapousidou, Alexandra Lanot

Supervision: Evangelos Daskalakis, Mohamed H. Hassan, Abdalla M. Omar, Paulo J.D.S. Bartolo

Validation: Evangelos Daskalakis, Mohamed H. Hassan, Abdalla M. Omar, Maria Kapousidou, Dino Freitas, Mehmet Cagirici, Alexandra Lanot, Paulo J.D.S. Bartolo

Visualization: Evangelos Daskalakis, Mohamed H. Hassan, Abdalla M. Omar
Writing – original draft: Evangelos Daskalakis, Mohamed H. Hassan, Abdalla M. Omar
Writing – review & editing: All authors

Ethics approval and consent to participate

Not applicable.

Consent for publication

Not applicable.

Availability of data

Data is available from the corresponding author upon reasonable request

References

1. Wang Y, Pereira FR, Peach C, Huang B, Vyas C, Bartolo P. Robotic *in situ* bioprinting for cartilage tissue engineering. *Int J Extreme Manuf.* 2023;5(3):032004. doi: 10.1088/2631-7990/acda67
2. Dwivedi R, Mehrotra D. 3D bioprinting and craniofacial regeneration. *J Oral Biol Craniofac Res*. 2020;10(4): 650-659. doi: 10.1016/j.jobcr.2020.08.011
3. Baptista R, Guedes M. Morphological and mechanical characterization of 3D printed PLA scaffolds with controlled porosity for trabecular bone tissue replacement. *Mater Sci Eng C*. 2021;118:111528. doi: 10.1016/j.msec.2020.111528
4. Loh QL, Choong C. Three-dimensional scaffolds for tissue engineering applications: role of porosity and pore size. *Tissue Eng Part B Rev*. 2013;19(6):485-502. doi: 10.1089/ten.teb.2012.0437
5. Rahmati M, Silva EA, Reseland JE, Heyward CA, Haugen HJ. Biological responses to physicochemical properties of biomaterial surface. *Chem Soc Rev*. 2020;49(15): 5178–5224. doi: 10.1039/D0CS00103A
6. Wang C, Huang W, Zhou Y, *et al.* 3D printing of bone tissue engineering scaffolds. *Bioact Mater*. 2020;5(1): 82-91. doi: 10.1016/j.bioactmat.2020.01.004
7. Ribas RG, Schatkoski VM, Montanheiro TLA, *et al.* Current advances in bone tissue engineering concerning ceramic and bioglass scaffolds: a review. *Ceram Int*. 2019;45(17):21051-21061. doi: 10.1016/j.ceramint.2019.07.096
8. Vyas C, Ates G, Aslan E, Hart J, Huang B, Bartolo B. Three-dimensional printing and electrospinning dual-scale polycaprolactone scaffolds with low-density and oriented fibers to promote cell alignment. *3D Print Addit Manuf*. 2020;7(3):105-113. doi: 10.1089/3dp.2019.0091
9. Huang B, Aslan E, Jiang Z, et al. Engineered dual-scale poly(ε-caprolactone) scaffolds using 3D printing and rotational electrospinning for bone tissue regeneration. *Addit Manuf.* 2020;36:101452. doi: 10.1016/j.addma.2020.101452
10. Caetano G, Violante R, Sant'Ana AB, *et al.* Cellularized versus decellularized scaffolds for bone regeneration. *Mater Lett*. 2016;182:318-322. doi: 10.1016/j.matlet.2016.05.152
11. Hassan MH, Omar AM, Daskalakis E, *et al.* The potential of polyethylene terephthalate glycol as biomaterial for bone tissue engineering. *Polymers*. 2020;12(12):3045. doi: 10.3390/polym12123045
12. Martins RF, Branco R, Martins M, *et al.* Mechanical properties of additively manufactured polymeric materials—PLA and PETG—for biomechanical applications. *Polymers*. 2024;16(13):1868. doi: 10.3390/polym16131868
13. Moreno Nieto D, Alonso-García M, Pardo-Vicente MA, Rodríguez-Parada L. Product design by additive manufacturing for water environments: study of degradation and absorption behavior of PLA and PETG. *Polymers*. 2021;13(7):1036. doi: 10.3390/polym13071036
14. Habibi Y, Lucia LA, Rojas OJ. Cellulose nanocrystals: chemistry, self-assembly, and applications. *Chem Rev*. 2010;110(6):3479-3500. doi: 10.1021/cr900339w
15. Saxena IM, Brown RM. Cellulose biosynthesis: current views and evolving concepts. *Ann Bot*. 2005;96(1):9–21. doi: 10.1093/aob/mci155
16. Bhatnagar A, Sain M. Processing of cellulose nanofiber-reinforced composites. *J Reinf Plast Compos*. 2005;24(12):1259-1268. doi: 10.1177/0731684405049864
17. Wu Q, Henriksson M, Liu X, Berglund LA. A high strength nanocomposite based on microcrystalline cellulose and polyurethane. *Biomacromolecules*. 2007;8(12):3687-3692. doi: 10.1021/bm701061t
18. Utoiu E, Manoiu VS, Oprita EI, Craciunescu O. Bacterial cellulose: a sustainable source for hydrogels and 3D-printed scaffolds for tissue engineering. *Gels*. 2024;10(6):387. doi: 10.3390/gels10060387
19. Shrivastav P, Pramanik S, Vaidya G, *et al.* Bacterial cellulose as a potential biopolymer in biomedical applications: a state-of-the-art review. *J Mater Chem B*. 2022;10(17): 3199-3241. doi: 10.1039/d1tb02709c

20. Torgbo S, Sukyai P. Biodegradation and thermal stability of bacterial cellulose as biomaterial: the relevance in biomedical applications. *Polym Degrad Stabil*. 2020;179:109232. doi: 10.1016/j.polymdegradstab.2020.109232

21. Wu Y, Wang Y, Wang F, Huang Y, He J. Preparation of 3D printed polylactic acid/bacterial cellulose composite scaffolds for tissue engineering applications. *Polymers*. 2022;14(21):4756. doi: 10.3390/polym14214756

22. Panaitescu MD, Frone NA, Chiulan I, Gabor RA, Spataru IC, Căşărică A. Biocomposites from polylactic acid and bacterial cellulose nanofibers obtained by mechanical treatment. *Bioresources*. 2017;12(1):662-672. doi: 10.15376/biores.12.1.662-672

23. Yodsanga S, Poeaim S, Chantarangsu S, Swasdison S. Investigation of biodegradation and biocompatibility of chitosan–bacterial cellulose composite scaffold for bone tissue engineering applications. *Cells*. 2025;14(10):723. doi: 10.3390/cells14100723

24. Saska S, Barud SH, Gaspar MMA, Marchetto R, Ribeiro SJL, Messaddeq Y. Bacterial cellulose-hydroxyapatite nanocomposites for bone regeneration. *Int J Biomater*. 2011;2011:1-8. doi: 10.1155/2011/175362

25. Boyetey BM, Torgbo S, Sukyai P. Bio-scaffold for bone tissue engineering with focus on bacterial cellulose, biological materials for hydroxyapatite synthesis and growth factors. *Eur Polym J*. 2023;194:112168. doi: 10.1016/j.eurpolymj.2023.112168

26. Wang X, Zhang Y, Luo J, *et al.* Printability of hybridized composite from maleic acid-treated bacterial cellulose with gelatin for bone tissue regeneration. *Adv Compos Hybrid Mater*. 2023;6:134. doi: 10.1007/s42114-023-00711-7

27. Lee CM, Gu J, Kafle K, Catchmark J, Kim SH. Cellulose produced by *Gluconacetobacter xylinus* strains ATCC 53524 and ATCC 23768: pellicle formation, post-synthesis aggregation and fiber density. *Carbohydr Polym*. 2015;133:270-276. doi: 10.1016/j.carbpol.2015.06.091

28. Yan C, Kleiner C, Tabigue A, *et al.* PETG: applications in modern medicine. *Eng Regen*. 2024;5(1):45-55. doi: 10.1016/j.engreg.2023.11.001

29. Daicho K, Kobayashi K, Fujisawa S, Saito T. Crystallinity-independent yet modification-dependent true density of nanocellulose. *Biomacromolecules*. 2019;21(2):939-945. doi: 10.1021/acs.biomac.9b01584

30. Saxena P, Shukla P, Gaur M. Thermal analysis of polymer blends and double layer by DSC. *Polym Polym Compos*. 2020;29(9):S11-S18. doi: 10.1177/0967391120984606

31. Martínez Cortizas A, López-Costas O. Linking structural and compositional changes in archaeological human bone collagen: an FTIR-ATR approach. *Sci. Rep.* 2020;10(1): 17888. doi: 10.1038/s41598-020-74993-y

32. Figueiredo M, Fernando A, Martins G, Freitas J, Judas F, Figueiredo H. Effect of the calcination temperature on the composition and microstructure of hydroxyapatite derived from human and animal bone. *Ceram Int*. 2010;36(8):2383–2393. doi: 10.1016/j.ceramint.2010.07.016

33. Zhu X, Chen T, Feng B, *et al.* Biomimetic bacterial cellulose-enhanced double-network hydrogel with excellent mechanical properties applied for the osteochondral defect repair. *ACS Biomater Sci Eng.* 2018;4(10):3534-3544. doi: 10.1021/acsbiomaterials.8b00682

34. Loskot J, Jezbera D, Loskot R, *et al.* Influence of print speed on the microstructure, morphology, and mechanical properties of 3D-printed PETG products. *Polym Test*. 2023;123:108055. doi: 10.1016/j.polymertesting.2023.108055

35. Aguayo MG, Fernández Pérez A, Reyes G, *et al.* Isolation and characterization of cellulose nanocrystals from rejected fibers originated in the Kraft pulping process. *Polymers*. 2018;10(10):1145. doi: 10.3390/polym10101145

36. Techawinyutham L, Tengsuthiwat J, Srisuk R, Techawinyutham W, Rangappa SM, Siengchin S. Recycled LDPE/PETG blends and HDPE/PETG blends: mechanical, thermal, and rheological properties. *J Mater Res Technol*. 2021;15:2445-2458. doi: 10.1016/j.jmrt.2021.09.052

37. Bhandari S, Lopez-Anido RA, Gardner DJ. Enhancing the interlayer tensile strength of 3D printed short carbon fiber reinforced PETG and PLA composites via annealing. *Addit Manuf*. 2019;30:100922. doi: 10.1016/j.addma.2019.100922

38. Rand B, Robinson R. Surface characteristics of carbon fibres from PAN. *Carbon*. 1977;15(4):257-263. doi: 10.1016/0008-6223(77)90011-2

39. Calore AR, Srinivas V, Groenendijk L, *et al.* Manufacturing of scaffolds with interconnected internal open porosity and surface roughness. *Acta Biomater*. 2023;156:158-176. doi: 10.1016/j.actbio.2022.07.017

40. Ahn J-H, Kim J, Han G, *et al.* 3D-printed biodegradable composite scaffolds with significantly enhanced mechanical properties via the combination of binder jetting and capillary rise infiltration process. *Addit Manuf*. 2021;41:101988. doi: 10.1016/j.addma.2021.101988

41. McAdam B, Fournet MB, McDonald P, Mojicevic M. Production of polyhydroxybutyrate (PHB) and factors impacting its chemical and mechanical characteristics. *Polymers*. 2020;12(12):2908. doi: 10.3390/polym12122908

42. Oh JE, Park N-M. Hydrophilic, transparent, and stretchable film using unmodified cellulose fibers. *Mater Lett.* 2022;309:131385. doi: 10.1016/j.matlet.2021.131385

43. Huang K, Zhu T, Nie J, *et al.* Microporous spongy scaffolds based on biodegradable elastic polyurethanes for the migration and growth of host cells. *ACS Appl Polym Mater.* 2022;4(5):3942-3951. doi: 10.1021/acsapm.2c00398

44. Zou M, Zhao X, Zhang X, Zhao Y, Zhang C, Shi K. Bio-inspired multiple composite film with anisotropic surface wettability and adhesion for tissue repair. *Chem Eng J.* 2020;398:125563. doi: 10.1016/j.cej.2020.125563

45. Conrad TL, Jaekel DJ, Kurtz SM, Roeder RK. Effects of the mold temperature on the mechanical properties and crystallinity of hydroxyapatite whisker-reinforced polyetheretherketone scaffolds. *J Biomed Mater Res B.* 2013;101(4):576-583. doi: 10.1002/jbm.b.32859

46. Bhattarai N, Li Z, Edmondson D, Zhang M. Alginate-based nanofibrous scaffolds: structural, mechanical, and biological properties. *Adv Mater.* 2006;18(11):1463-1467. doi: 10.1002/adma.200502537

47. Hassan MH, Omar AM, Daskalakis E, Liu F, Bartolo P. Preliminary studies on the suitability of PETG for 4D printing applications. MATEC Web Conf. 2020;318:01010. doi: 10.1051/matecconf/202031801010

48. Lanyi FJ, Wenzke N, Kaschta J, Schubert DW. On the determination of the enthalpy of fusion of α-crystalline isotactic polypropylene using differential scanning calorimetry, X-ray diffraction, and Fourier-transform infrared spectroscopy: an old story revisited. *Adv Eng Mater.* 2019;22(9):1900796. doi: 10.1002/adem.201900796

49. Paszkiewicz S, Szymczyk A, Pawlikowska D, *et al.* Synthesis and characterization of poly(ethylene terephthalate-co-1,4-cyclohexanedimethylene terephthalate)-block-poly(tetramethylene oxide) copolymers. *RSC Adv.* 2017;7(66):41745-41754. doi: 10.1039/c7ra07172h

50. Atykyan N, Revin V, Shutova V. Raman and FT-IR spectroscopy investigation of the cellulose structural differences from bacteria gluconacetobacter sucrofermentans during different regimes of cultivation on a molasses media. *AMB Express.* 2020;10(1):84. doi: 10.1186/s13568-020-01020-8

51. Bagwan JK, Ahuja BB, Mulay AV, Jawale KJ. Geometrical analysis of extrusion-based (additively manufactured) 3D designed scaffold for bone tissue engineering: a finite element approach, *Mater Today Proc.* 2022;50(5):1465-1471. doi: 10.1016/j.matpr.2021.09.049

52. Yao Y, Chen S. The effects of fiber's surface roughness on the mechanical properties of fiber-reinforced polymer composites. *J. Compos. Mater.* 2012;47(23):2909-2923. doi: 10.1177/0021998312459871

53. Shuai C, Wang C, Qi F, *et al.* Enhanced crystallinity and antibacterial of PHBV scaffolds incorporated with zinc oxide. *J Nanomater.* 2020:1-12. doi: 10.1155/2020/6014816

54. Wang G, Qi F, Yang W, *et al.* Crystallinity and reinforcement in poly-L-lactic acid scaffold induced by carbon nanotubes. *Adv Polym Technol.* 2019:1-10. doi: 10.1155/2019/8625325

55. Huang B, Wang Y, Vyas C, Bartolo B. Crystal growth of 3D poly(ε-caprolactone) based bone scaffolds and its effects on the physical properties and cellular interactions. *Adv Sci.* 2020;10(1):2203183. doi: 10.1002/advs.202203183

56. Ustunel S, Prévôt ME, Webb G, *et al.* Mechanically tunable elastomer and cellulose nanocrystal composites as scaffolds for in vitro cell studies. *Mater Adv.* 2021;2(1):464-476. doi: 10.1039/d0ma00676a

57. Lužanin O, Gudurić V, Bernhardt A, *et al.* Impact of in-process crystallinity of biodegradable scaffolds fabricated by material extrusion on the micro- and nanosurface topography, viability, proliferation, and differentiation of human mesenchymal stromal cells. *Polymers.* 2023;15(6):1468. doi: 10.3390/polym15061468

58. Wen JH, Vincent LG, Fuhrmann A, *et al.* Interplay of matrix stiffness and protein tethering in stem cell differentiation. *Nat Mater.* 2014;13(10):979-987. doi: 10.1038/nmat4051

59. Morgan EF, Unnikrisnan GU, Hussein AI. Bone mechanical properties in healthy and diseased states. *Annu Rev Biomed Eng.* 2018;20:119-143. doi: 10.1146/annurev-bioeng-062117-121139

60. Öhman-Mägi C, Holub O, Wu D, Hall RM, Persson C. Density and mechanical properties of vertebral trabecular bone—a review. *JOR Spine.* 2021;4(4):e1176. doi: 10.1002/jsp2.1176